sustainability

MDPI

Article

A High-Gain DC Side Converter with a Ripple-Free Input Current for Offshore Wind Energy Systems

Ran Tao [1], Jingpeng Yue [1], Zhenlin Huang [1], Ranran An [1], Zou Li [2] and Junfeng Liu [2,*]

[1] Guangdong Key Laboratory of New Technology for Smart Grid, Guangzhou 510062, China
[2] School of Automation Science and Engineering, South China University of Technology, Guangzhou 510641, China
* Correspondence: jf.liu@connect.polyu.hk

Abstract: Considering that the distance between offshore wind farms and onshore converters is getting farther and farther, dc transmission becomes increasingly more applicable than conventional ac transmission. To reduce the transmission loss, a feasible solution is using a high-gain dc/dc converter to boost the rectified output voltage to thousands of volts. Thus, a novel single-switch high-gain dc/dc converter with a ripple-free input current is presented in this paper. The structure consists of two cells—a coupled-inductor cell and a switched-capacitor cell. The coupled-inductor cell in the proposed converter provides a ripple-free input current. The switched-capacitor cell provides a high voltage gain. The converter has a simple control strategy due to the use of a single switch. Moreover, the output capacitor is charged and discharged continuously by a 180° phase shift to eliminate the output voltage ripple. A steady-state analysis of the converter is proposed to determine the parameters of the devices. In addition, a 240 W, 40/308 V laboratory prototype at 35 kHz switching frequency has been developed, in which the input current ripple is only 1.1% and a peak efficiency of 94.5% is reached. The experimental results verify the validity and feasibility of the proposed topology.

Keywords: dc/dc converter; high voltage gain; ripple-free input current; offshore wind farms

check for updates

Citation: Tao, R.; Yue, J.; Huang, Z.; An, R.; Li, Z.; Liu, J. A High-Gain DC Side Converter with a Ripple-Free Input Current for Offshore Wind Energy Systems. *Sustainability* **2022**, *14*, 11574. https://doi.org/10.3390/su141811574

Academic Editors: Wenbin Yu and Guang Zeng

Received: 19 August 2022
Accepted: 8 September 2022
Published: 15 September 2022

Publisher's Note: MDPI stays neutral with regard to jurisdictional claims in published maps and institutional affiliations.

Copyright: © 2022 by the authors. Licensee MDPI, Basel, Switzerland. This article is an open access article distributed under the terms and conditions of the Creative Commons Attribution (CC BY) license (https://creativecommons.org/licenses/by/4.0/).

1. Introduction

With the beginning of global carbon neutrality, offshore wind energy has become one of the main and growing sources of renewable energy worldwide [1–3]. The European Commission stated that the offshore wind power capacity in Europe would reach 450 GW by 2050, making it a key part of renewable energy [4]. Compared with its onshore counterpart, an offshore wind farm has the merits of less land occupation, higher wind speeds, and more stable wind conditions [5–7]. However, there are some problems that need to be solved, such as the difficulties of installation and maintenance [8,9]. Once an accident occurs, the long time for fault correction will have an adverse impact on the continuous power supply. Moreover, with the increase in offshore distance, conventional high voltage ac (HVAC) transmission is no longer suitable for long-distance offshore wind farms, as it brings higher power loss and significant power fluctuation [10–12].

Considering the above problems, high voltage dc (HVDC) transmission appears to be a more promising solution for long-distance and large-scale offshore wind farms [13–15]. The traditional HVAC transmission system of an offshore wind farm consists of a medium voltage ac (MVAC) collection grid as shown in Figure 1. Each wind turbine is connected to a transformer to boost the turbine's output voltage. To avoid the use of large volume transformers, a HVDC transmission system uses a medium voltage dc (MVDC) collection grid as shown in Figure 2 [16–18], where the traditional MV transformers are replaced by MV step-up dc/dc converters. The use of MV dc/dc converters can significantly reduce the volume and weight of the offshore platforms which leads to lower installation costs. Meanwhile, due to the low output voltage generated by wind turbines, high-gain dc/dc converters become one of the key levels of MV dc collection grids [19–21]. In the existing research, there are bidirectional and unidirectional high-gain dc/dc converters. However, there is no need for bidirectional power flow capacity due to the inherent characteristics of offshore wind farms, so a simpler unidirectional dc/dc converter is more applicable for offshore wind energy systems [22]. In addition to a high voltage gain, there are some other challenges such as low input current ripple, high conversion efficiency, and high-power density. To overcome these challenges, a large amount of relevant research has been done.

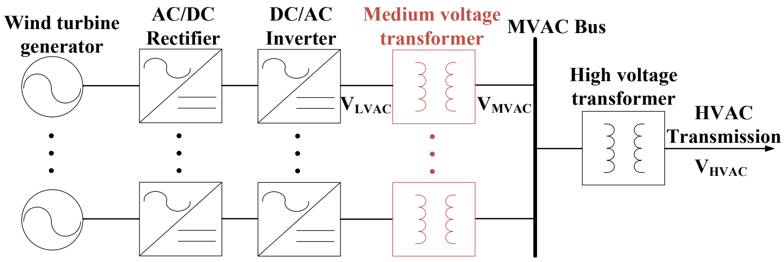

Figure 1. HVAC transmission system with MVAC grid.

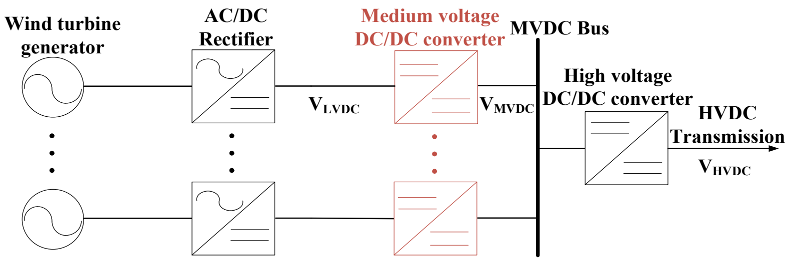

Figure 2. HVDC transmission system with MVDC grid.

To reduce the power loss and maintain high efficiency, researchers have generated much interest in high-gain dc/dc converters for offshore wind farms. In [23], a high-gain resonant switched-capacitor (RSC) dc/dc converter was introduced, which provided low switching losses and high efficiency by the resonant switching transitions. In addition, the voltage gain was increased through the series-modular configuration. However, to reach a high voltage gain, lots of switching devices and passive components were used in the topology. Meanwhile, the voltage stress increment of the switches and diodes blocked its application in offshore wind energy systems. To reduce the number of power switches, [24,25] both presented step-up dc/dc converters which worked only by one switch. The control of the converters was easy, and the conduction loss of the switch was decreased due to the use of a single-switch structure. But the voltage gain was not high enough. In [26], a high-power multilevel step-up dc/dc converter was studied with the merits of outstanding dynamic performance and low voltage stress. Although there was a filter inductor in this converter that could reduce the input current ripple, the step-up ratio was not high enough for offshore wind farms. Moreover, the concept of modularization used in offshore wind farms has attracted considerable interests recently due to its high reliability and excellent expandability [27–30]. Nevertheless, a complex switching scheme is usually required in the modular structure. Furthermore, a large number of power devices connected in series increase the volume and weight of the offshore platforms and may raise the overall costs.

In order to ensure the long-distance and stable transmission of electricity, a ripple-free input current is necessary for a high-gain dc/dc converter. Generally, bulky and huge electrolytic capacitors are used at the input stage of the dc/dc converters to decrease the large input current ripple. To avoid the use of bulky electrolytic capacitors, a filter inductor is placed at the input stage to reduce the current ripple [31]. However, the current ripple still exists, and the effect is not ideal. By utilizing the interleaved structure of switches and inductors on the input side, the input current ripple was significantly reduced in [32]. Nevertheless, the switching scheme is relatively complex and the input direct current still consists of a little ripple. An improved dc/dc converter with a ripple-free input current was proposed in [33]. The input current ripple was reduced to zero with the use of the coupled inductor. Moreover, the converter can reach a high voltage gain through the use of a transformer. However, the use of too many magnetic components also limits its application in offshore wind farms due to the increase in volume and weight. Nonetheless, the coupled inductor is a promising component to achieve a ripple-free input current.

Considering the above problems, this paper presents a single-switch high-gain dc/dc converter with a ripple-free input current. The proposed converter combines the coupled inductor with the switch-capacitor structure and has the following features by comparing with the existing converters: (1) high voltage gain; (2) ripple-free input current; (3) simplicity of control strategy; (4) low voltage stress across the components; (5) high efficiency. Given all of the advantages, the converter is very suitable for offshore wind energy systems.

The rest of this paper is organized as follows. The proposed topology and operating principle are discussed in Section 2. The detailed steady-state analysis is presented in Section 3. The performance comparisons of the converters are provided in Section 4. Section 5 illustrates the parameters design and the selection of the components. Experimental results are shown in Section 6. Finally, conclusions are drawn in Section 7.

2. Topology and Operating Principle

2.1. Topology

Figure 3a shows the proposed single-switch dc/dc converter with a high voltage gain and a ripple-free input current. A coupled inductor L_C is inserted at the input stage to eliminate the input current ripple. Figure 3b shows the equivalent circuit of the converter where the coupled inductor L_C is described by the magnetic inductor L_m, the leakage inductor L_k, and the ideal transformer (turns ratio $n = N_s/N_p$). The switched-capacitor cell uses only one switch with a new arrangement of the diodes and capacitors to raise the voltage gain significantly. The control strategy is very simple due to the use of one switch which can reduce the incidence of failure in offshore wind energy systems. The theoretical waveforms of the main devices are shown in Figure 4. The voltage at both ends of the primary side and the secondary side of the coupled inductor are defined as v_p and v_s, respectively. The analysis of the converter during a switching period T_S can be divided into two operating modes, and they are shown in Figure 5.

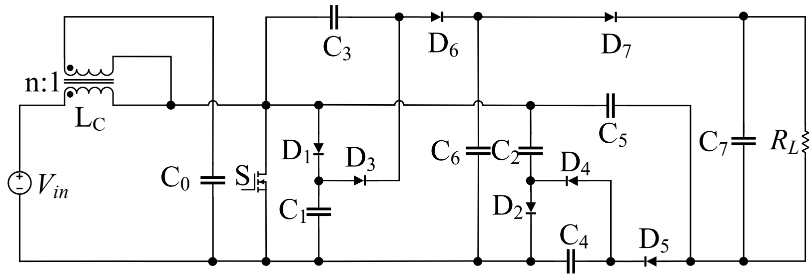

(**a**)

Figure 3. *Cont.*

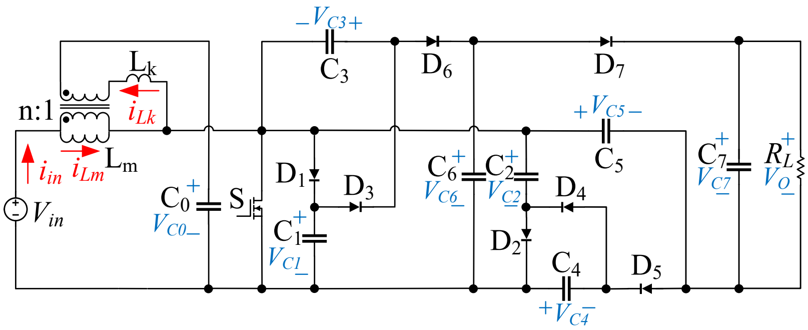

(**b**)

Figure 3. Proposed dc/dc converter: (**a**) Topology; (**b**) Equivalent circuit.

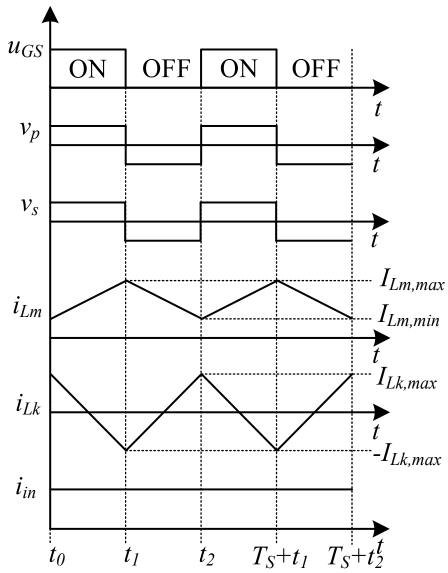

Figure 4. Theoretical waveforms of the proposed converter.

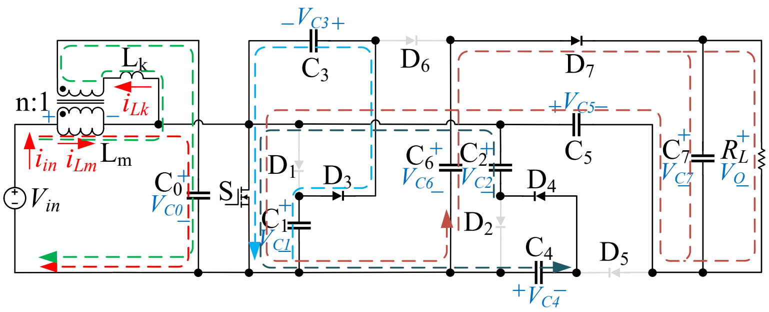

(**a**)

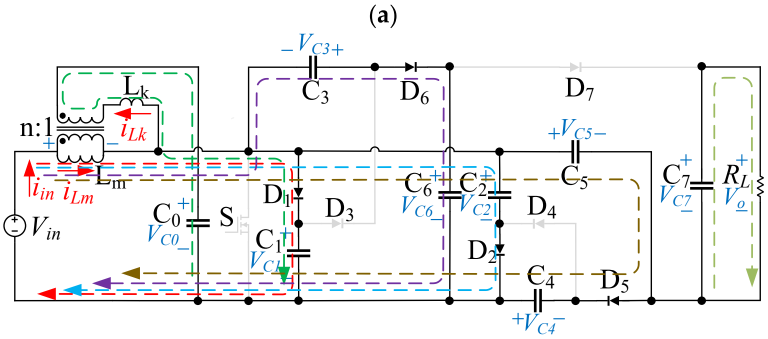

(**b**)

Figure 5. Operating modes of the proposed converter: (**a**) Mode 1; (**b**) Mode 2.

2.2. Operating Principle

Since the circuit is controlled by one switch, there are only two operating modes during a switching period. The following assumptions are made before the analysis.

(1) All the switches, capacitors, diodes, and inductors used in the circuit are assumed to be ideal components;
(2) All the capacitors are large enough to maintain output voltage constant;
(3) V_{in} is an ideal dc voltage source, and the load is modeled by a pure resistor R_L.

Mode 1 [t_0,t_1] in Figure 5a: In this mode, the switch S begins to conduct under the action of the gate driving signal. The current i_{Lm} increases linearly from its minimum value due to the positive voltage. The diodes D_1, D_2, D_5, and D_6 are reverse biased. The magnetic inductor L_m starts to be charged by the input voltage source V_{in}. C_1 is discharged to C_3 through diode D_3 and C_2 is discharged to C_4 through diode D_4. Meanwhile, C_5 and C_6 are discharged in series to C_7 and R_L through diode D_7. Figure 6 shows the simplified equivalent circuits in this mode.

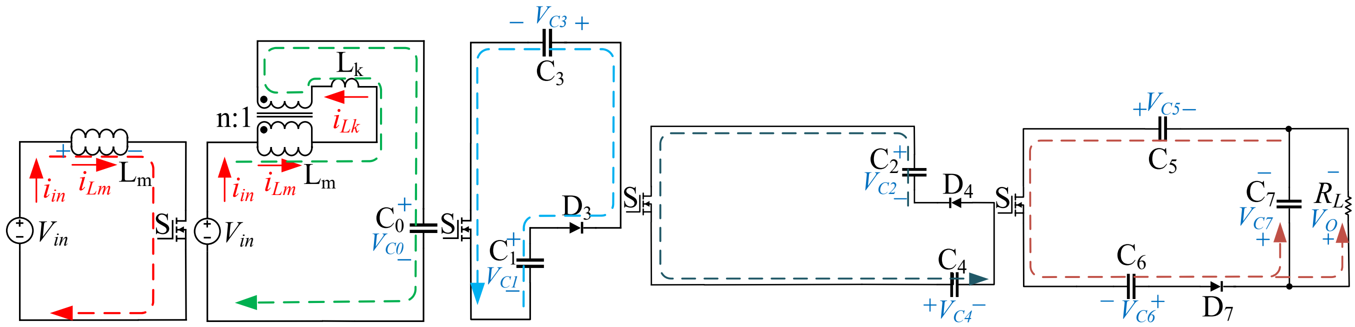

Figure 6. Simplified equivalent circuits of Mode 1.

Here, the voltages across the capacitors, diodes, inductor, and load are defined as V_{C0}–V_{C7}, V_{D1}–V_{D7}, v_{Lm}, v_{Lk}, and V_O, respectively. Similarly, the currents flowing through the input voltage source, magnetic inductor, and leakage inductor are defined as i_{in}, i_{Lm}, and i_{Lk}, respectively.

Mode 2 [t_1,t_2] in Figure 5b: At t_1, the switch S is turned off. The diodes D_3, D_4, and D_7 are reverse biased. The input voltage source V_{in} and magnetic inductor L_m are discharged in series to C_1 and C_2, respectively. Meanwhile, the input voltage source V_{in}, magnetic inductor L_m, and C_4 are discharged in series to C_5 through diode D_5. The input voltage source V_{in}, magnetic inductor L_m, and C_3 are discharged in series to C_6 through diode D_6. Therefore, the current i_{Lm} starts to decrease linearly from its maximum value, and the output capacitor C_7 is discharged to the load R_L. This mode ends when the driving signal of the switch S comes in the next period. Figure 7 shows the simplified equivalent circuits in this mode.

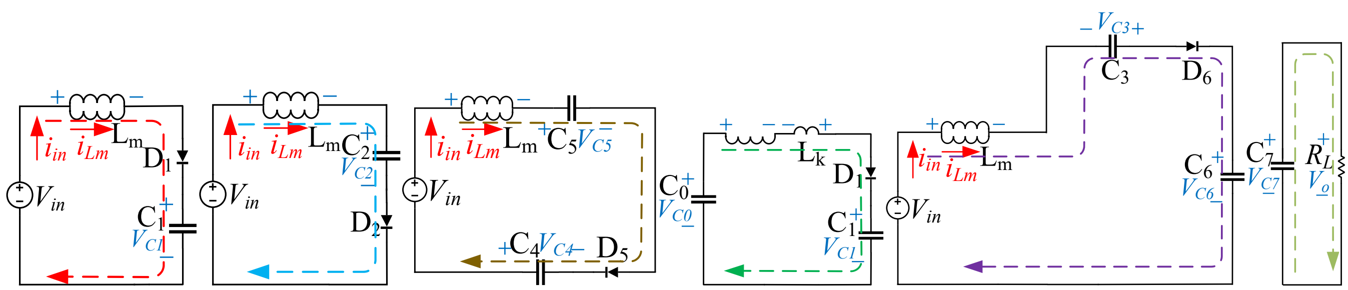

Figure 7. Simplified equivalent circuits of Mode 2.

3. Steady-State Analysis

3.1. Voltage Gain

Referring to Figures 5a and 6, when the switch is turned on, the following equations can be obtained according to Kirchhoff's voltage law, where $v_{Lm(on)}$ is the voltage across the magnetic inductor when the switch is turned on.

$$\begin{cases} v_{\mathrm{Lm}(on)} = V_{in} \\ V_{C3} = V_{C1} \\ V_{C4} = V_{C2} \\ V_{C5} + V_{C6} = V_{C7} = V_O \end{cases} \tag{1}$$

Similarly, from Figures 5b and 7, the voltage relationship of each loop can be expressed as follows, where $v_{Lm(off)}$ is the voltage across the magnetic inductor when the switch is turned off.

$$\begin{cases} V_{in} - v_{\mathrm{Lm}(off)} = V_{C1} = V_{C2} \\ V_{in} - v_{\mathrm{Lm}(off)} + V_{C4} = V_{C5} \\ V_{in} - v_{\mathrm{Lm}(off)} + V_{C3} = V_{C6} \\ V_O = V_{C7} \end{cases} \tag{2}$$

By applying the volt-second balance principle to the magnetic inductor L_m under steady-state conditions, the equation is given below:

$$\int_{t_0}^{t_0+T_S} v_{Lm} dt = 0 \tag{3}$$

where v_{Lm} is the voltage across the magnetic inductor.

From (1)–(3), the steady-state voltage expressions of the capacitors and the load are given below, where D is the duty cycle.

$$\begin{cases} V_{C1} = V_{C2} = V_{C3} = V_{C4} = \frac{V_{in}}{1-D} \\ V_{C5} = V_{C6} = \frac{2V_{in}}{1-D} \\ V_O = V_{C7} = \frac{4V_{in}}{1-D} \end{cases} \tag{4}$$

Therefore, the voltage gain M of the proposed converter can be derived as follows:

$$M = \frac{V_O}{V_{in}} = \frac{4}{1-D} \tag{5}$$

3.2. Ripple-Free Condition

As shown in Figure 5, the direction of the current can be obtained. From Figure 5a, when the switch S is turned on, the voltage v_{Lm} across L_m is V_{in}. Hence, the current i_{Lm} increases linearly from its minimum value $I_{Lm,min}$ as follows:

$$i_{Lm}(t) = I_{Lm,\mathrm{min}} + \int_{t_0}^{t} \frac{V_{in}}{L_m} dt \tag{6}$$

The voltage v_{Lk} across L_k is $-(V_{C0} - nV_{in})$. Therefore, the current i_{Lk} decreases linearly from its maximum value $I_{Lk,max}$ as follows:

$$i_{Lk}(t) = I_{Lk,\mathrm{max}} - \int_{t_0}^{t} \frac{V_{C0} - nV_{in}}{L_k} dt \tag{7}$$

Since the average inductor voltage must be zero under the steady-state conditions, the voltage V_{C0} can be shown as follows:

$$V_{C0} = V_{in} \tag{8}$$

It is apparent that the input current i_{in} is the sum of i_{Lm} and ni_{Lk}. Therefore, combining (6)–(8), i_{in} can be derived as follows:

$$i_{in}(t) = I_{Lm,\min} + nI_{Lk,\max} + \int_{t_0}^{t} (\frac{1}{L_m} - \frac{n(1-n)}{L_k})V_{in}dt \tag{9}$$

To achieve a ripple-free condition, the variation of input current must be zero during this stage as follows:

$$\frac{d}{dt}i_{in}(t) = 0 \tag{10}$$

From (9) and (10), since ($I_{Lm,min}$ + $nI_{Lk,max}$) is a constant value, the input current ripple is eliminated with the following condition:

$$L_k = n(1-n)L_m \tag{11}$$

Consequently, the input current i_{in} in Mode 1 is only determined by

$$i_{in}(t) = I_{Lm,\min} + nI_{Lk,\max} \tag{12}$$

Similarly, with the turn-off of the switch S shown in Figure 5b, the voltage v_{Lm} across L_m is $-(V_{C1} - V_{in})$. The current i_{Lm} decreases linearly from its maximum value $I_{Lm,max}$ as follows:

$$i_{Lm}(t) = I_{Lm,\max} - \int_{t_1}^{t} \frac{V_{C1} - V_{in}}{L_m}dt \tag{13}$$

The voltage v_{Lk} across L_k is ($V_{C1} - V_{C0}$ + nv_{Lm}), which can also be written as $(1 - n)$ $(V_{C1} - V_{in})$. Therefore, the current i_{Lk} increases linearly from its minimum value $-I_{Lk,max}$ as follows:

$$i_{Lk}(t) = -I_{Lk,\max} + \int_{t_1}^{t} \frac{(1-\mathrm{n})(V_{C1} - V_{in})}{L_k}dt \tag{14}$$

Combining (13) and (14), the input current i_{in} can be derived as follows:

$$i_{in}(t) = I_{Lm,\max} - nI_{Lk,\max} + \int_{t_1}^{t} (\frac{n(1-\mathrm{n})}{L_k} - \frac{1}{L_m})\frac{DV_{in}}{1-D}dt \tag{15}$$

Since ($I_{Lm,max} - nI_{Lk,max}$) is a constant value, the input current ripple is also eliminated with the condition of (11). Therefore, the input current i_{in} in Mode 2 is only determined by

$$i_{in}(t) = I_{Lm,\max} - nI_{Lk,\max} \tag{16}$$

From Figures 4 and 5a, the value of Δi_{Lm} can be obtained as follows:

$$\Delta i_{Lm} = I_{Lm,\max} - I_{Lm,\min} = \frac{V_{in}}{L_m}DT_S \tag{17}$$

From (7), (8), and Figure 4, the maximum value $I_{Lk,max}$ can be derived as follows:

$$I_{Lk,\max} = \frac{(1-\mathrm{n})V_{in}}{2L_k}DT_S \tag{18}$$

Combining (11), (17), and (18), $I_{Lk,max}$ can be further expressed by

$$I_{Lk,\max} = \frac{1}{2n}\frac{V_{in}}{L_m}DT_S = \frac{1}{2n}(I_{Lm,\max} - I_{Lm,\min}) \tag{19}$$

From (19), it can be concluded that

$$i_{in}(t) = I_{Lm,\min} + nI_{Lk,\max} = I_{Lm,\max} - nI_{Lk,\max} \tag{20}$$

Consequently, the input current i_{in} is a constant value during the whole switching period with the condition of (11).

3.3. Voltage Stress Analysis

Referring to the circuit diagrams shown in Figure 5 and according to Kirchhoff's voltage law, the following voltage relationships can be obtained:

$$\begin{cases} V_{DS} = V_{D1} = V_{C1} \\ V_{D2} = V_{D4} = V_{C4} \\ V_{D3} = V_{C3} \\ V_{D5} = V_{C5} - V_{C2} \\ V_{D6} = V_{C6} - V_{C1} \\ V_{D7} = V_{C7} - V_{C4} - V_{C6} \end{cases} \tag{21}$$

where V_{DS} and V_{D1}~V_{D7} are the voltage stresses of the switch S and the diodes D_1~D_7, respectively.

From (4), the simplified voltage stress relationship is given as follows:

$$V_{DS} = V_{D1} = V_{D2} = V_{D3} = V_{D4} = V_{D5} = V_{D6} = V_{D7} = \frac{V_{in}}{1-D} \tag{22}$$

Therefore, all the diodes and the switch have the same voltage stress which means the same type of diodes can be selected. Due to the relatively low voltage stress, the components with a lower-rated voltage and a lower on-resistance can be used to further reduce the power losses and costs.

3.4. Real-Gain Analysis

In fact, all the active and passive components contain some non-idealities in practice that influence the voltage gain and efficiency of high-gain dc/dc converters. Figure 8 shows the equivalent circuits of the proposed topology considering all the non-idealities in the two operating modes. In Figure 8, R_{Lp} and R_{Ls} are the equivalent series resistance (ESR) of the primary and secondary sides of the coupled inductor, respectively, R_{C0}–R_{C7} are the ESRs of capacitors, R_{D1}–R_{D7} are the forward diode resistances of diodes, V_{d1}–V_{d7} are the forward voltage drops of diodes, and R_S is the on-state resistance of the switch.

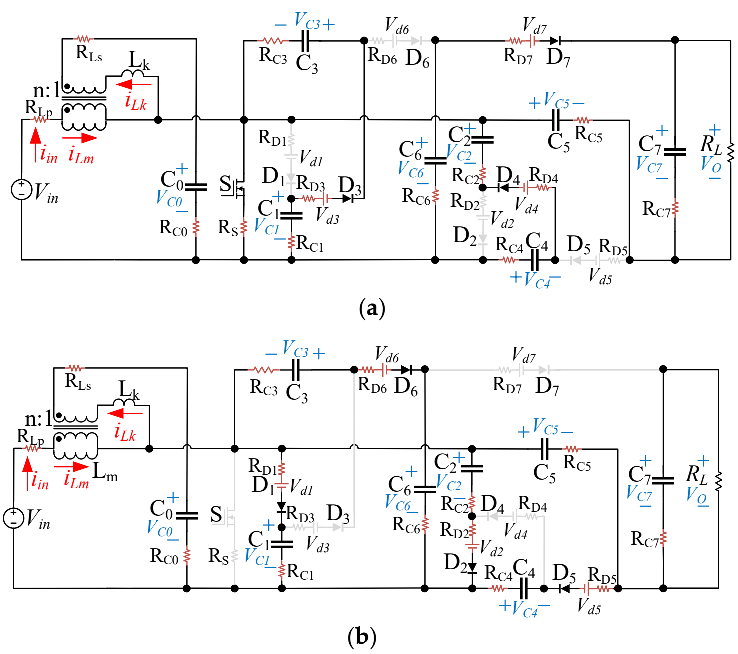

(**a**)

(**b**)

Figure 8. The equivalent circuits considering all the non-idealities: (**a**) Mode 1; (**b**) Mode 2.

Referring to Figure 8a, when the switch is turned on, the following equations can be obtained according to Kirchhoff's voltage law.

$$\begin{cases} v_{\mathrm{Lm}(on)} + i_{in}R_{Lp} = V_{in} \\ V_{C3} = V_{C1} - i_S R_S - i_{D3}(R_{C1} + R_{C3} + R_{D3}) - V_{d3} \\ V_{C4} = V_{C2} - i_S R_S - i_{D4}(R_{C2} + R_{C4} + R_{D4}) - V_{d4} \\ V_{C7} = V_{C5} + V_{C6} - i_S R_S - i_{D7}(R_{C5} + R_{C6} + R_{C7} + R_{D7}) - V_{d7} \end{cases} \tag{23}$$

Similarly, from Figure 8b, the voltage relationship of each loop can be expressed as follows when the switch is turned off.

$$\begin{cases} V_{C1} = V_{in} - v_{Lm(off)} - i_{in}R_{Lp} - i_{D1}(R_{C1} + R_{D1}) - V_{d1} \\ V_{C2} = V_{in} - v_{Lm(off)} - i_{in}R_{Lp} - i_{D2}(R_{C2} + R_{D2}) - V_{d2} \\ V_{C5} = V_{in} - v_{Lm(off)} + V_{C4} - i_{in}R_{Lp} - i_{D5}(R_{C4} + R_{C5} + R_{D5}) - V_{d5} \\ V_{C6} = V_{in} - v_{Lm(off)} + V_{C3} - i_{in}R_{Lp} - i_{D6}(R_{C3} + R_{C6} + R_{D6}) - V_{d6} \\ V_O = V_{C7} - i_O R_{C7} \end{cases} \tag{24}$$

By applying the volt-second balance principle to the magnetic inductor L_m, the real-gain of the proposed converter can be deduced and is given below after simplification.

$$V_O = \frac{1}{H} \cdot \left[V_{in} - \frac{1-D}{4}(V_{d1} + V_{d2} + V_{d3} + V_{d4} + V_{d5} + V_{d6} + V_{d7}) \right] \tag{25}$$

where the parameter H is defined as follows:

$$H = \frac{1-D}{4} + \frac{4R_{Lp}}{(1-D)R_L} + \frac{(3+D)R_S}{4R_L} + \frac{1-D}{4R_L} \cdot \begin{bmatrix} (R_{D1} + R_{D2} + R_{D3} + R_{D4} + R_{D5} + R_{D6} + R_{D7}) + \\ 2(R_{C1} + R_{C2} + R_{C3} + R_{C4} + R_{C5} + R_{C6} + R_{C7}) \end{bmatrix} \tag{26}$$

3.5. Losses Analysis

The power losses of the proposed converter are caused by diodes, capacitors, the switch, and the coupled inductor.

In the diodes D_1-D_7, the forward voltage drop and forward resistance are the reasons for the power loss $P_{D,}$ and it can be derived as follows:

$$P_D = V_d I_D + R_D {I_D}^2 \tag{27}$$

where V_d, R_D, and I_D are the forward voltage drop, the forward resistance, and the average current of the diodes, respectively.

As for capacitors C_0–C_7, the power loss P_C caused by the ESR can be calculated by

$$P_C = \frac{f_S \cdot C \cdot \Delta U^2}{2} \tag{28}$$

where C and ΔU represent the capacitance and voltage ripple of the capacitor, respectively.

As for switch S, the power losses comprise conduction loss $P_{S\text{-}C}$ and switching loss $P_{S\text{-}S}$. The on-resistance is the reason for the conduction loss of a switch. By defining the on-resistance and rms current of the switch as R_{DSon} and I_S, respectively, the conduction loss $P_{S\text{-}C}$ can be obtained as follows:

$$P_{S\_C} = {I_S}^2 R_{DSon} \tag{29}$$

The switching loss $P_{S\text{-}S}$ can be estimated by linearizing the voltage and current of the switch during the turn-on and turn-off processes as follows:

$$\begin{cases} P_{S\_S_{ON}} = V_{DS} \cdot I_{on} \cdot t_{ondelay} \cdot f_S/6 \\ P_{S\_S_{OFF}} = V_{DS} \cdot I_{off} \cdot t_{offdelay} \cdot f_S/6 \end{cases} \tag{30}$$

where I_{on} and I_{off} are the turn-on and turn-off currents, and $t_{ondelay}$ and $t_{offdelay}$ are the turn-on and turn-off time delays.

As for the coupled inductor, the power losses are mainly composed of copper loss $P_{L\text{-}copper}$ and core loss $P_{L\text{-}core}$. According to [34], the theoretical estimation formula of copper loss can be obtained as follows:

$$P_{L\_copper} = {I_L}^2 r_L \tag{31}$$

where I_L and r_L represent the rms current and the ESR of the coupled inductor, respectively.

The core loss can be calculated by

$$P_{L\_core} = K_{Fe} \cdot V_e \cdot f_S \cdot \left(\frac{\Delta B}{2}\right)^{\alpha} \tag{32}$$

where K_{Fe} and α are constants determined by the core material, V_e is the volume of the core, and ΔB is decided by the current ripple of the coupled inductor.

The total power loss of the proposed converter can be obtained as follows:

$$P_{total} = P_D + P_C + P_{S\_C} + P_{S\_S_{ON}} + P_{S\_S_{OFF}} + P_{\text{L\_copper}} + P_{\text{L\_core}} \tag{33}$$

In order to exhibit the losses distribution of the proposed converter intuitively, the losses of each component at 240 W are calculated through (27)–(32) and shown graphically in Figure 9. It can be seen that most of the total power loss occurs in the diodes, which is mainly caused by the large output current. However, the conduction loss of the switch is significantly reduced due to the use of a single switch compared with other multi-switch high-gain converters.

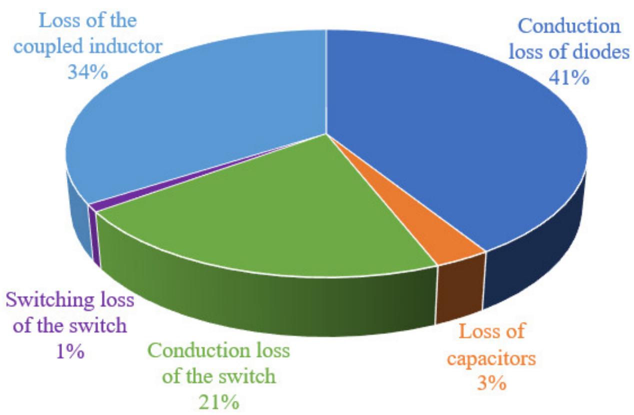

Figure 9. Loss distribution of the proposed converter.

4. Performance Comparisons

The performance indexes of relevant high-gain dc/dc converters are summarized in Table 1, including the number of switches, voltage gain, voltage stress of switches and diodes, total standing voltage (TSV), and input current ripple. According to [35], the total voltage rating of switching power devices can be reflected by TSV which is defined as

$$TSV = \frac{\sum_{i=1}^{n} V_{Sn} + \sum_{j=1}^{m} V_{Dj}}{V_o} \tag{34}$$

where V_{Sn} and V_{Dj} represent the voltage stress of each switch and diode, respectively.

Table 1. Comparisons among different converters.

Parameters	[24]	[25]	[26]	[32]	Proposed
Number of switches	1	1	3	2	1
Voltage gain	$\frac{3D}{1-D}$	$\frac{3+D}{2(1-D)}$	$\frac{1+D}{1-D}$	$\frac{D(1+D)}{(1-D)^2}$	$\frac{4}{1-D}$
Voltage stress of switches	$\frac{V_O}{3D}$	$\frac{2V_O}{3+D}$	$\frac{V_O}{3(1+D)}$	$\frac{V_O}{1+D}$, $\frac{(1-D)V_O}{D(1+D)}$	$\frac{V_O}{4}$
Voltage stress of diodes	$\frac{V_O}{3D}$	$\frac{V_O}{3+D}$, $\frac{2V_O}{3+D}$	$\frac{V_O}{3(1+D)}$	$\frac{V_O}{1+D}$, $\frac{(1-D)V_O}{D(1+D)}$	$\frac{V_O}{4}$
TSV	$\frac{4}{3D}$	$\frac{8}{3+D}$	$\frac{3}{1+D}$	$\frac{2+D}{D(1+D)}$	2
Input current ripple	Low	High	High	Low	Zero

Figure 10 gives the comparison curves of different converters in Table 1. From Figure 10a, the proposed converter has the highest voltage-boosting capability compared to other converters in the optimal duty cycle range. From Table 1, the switches and diodes of all the converters have the same maximum voltage stress. Thus, the maximum voltage stress curve of switches and diodes is plotted in Figure 10b. The voltage stress in the proposed converter is lower than other converters except for the converter in [26]. Although the voltage stress in [26] is lower when the duty cycle is greater than 1/3, its voltage gain is much lower than that in the proposed converter. Similarly, Figure 10c shows that the proposed converter has the lowest TSV when the duty cycle is smaller than 0.5. The TSV in [26] is lower than that in this paper when the duty cycle is greater than 0.5; however, its voltage gain is also much lower. It can be deduced from Table 1 and Figure 10 that the proposed converter has a high voltage gain and a low voltage stress. That is to say, the active power devices with low withstand voltage can be selected.

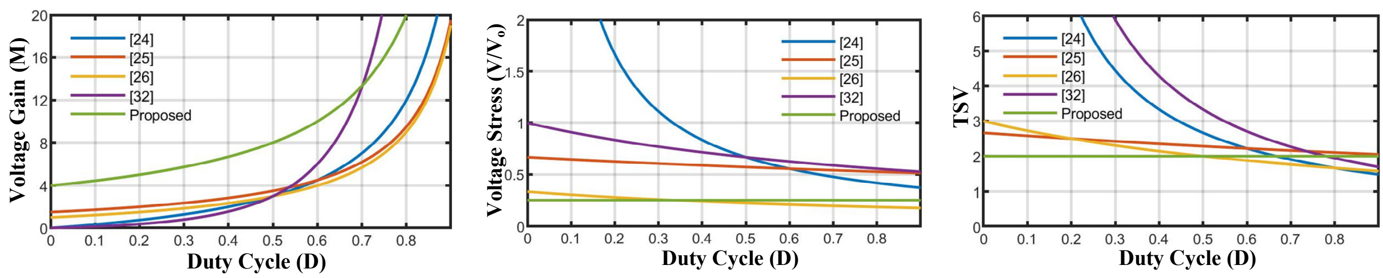

(**a**) (**b**) (**c**)

Figure 10. Comparative results of the converters versus the duty cycle D: (**a**) Voltage gain; (**b**) Voltage stress of switches and diodes; (**c**) TSV.

Moreover, from Table 1, the number of switches used in [24,25] and the proposed converter is the smallest. The proposed converter uses only one switch which can significantly simplify the control strategy. Meanwhile, the proposed converter has the lowest input current ripple, and it achieves a ripple-free input current condition which is of great importance in offshore wind energy systems. Owing to the ripple-free input current, the HVDC transmission will be more stable. Consequently, the proposed converter is well suited for offshore wind farms due to the above-mentioned superiorities.

5. Design Guideline

5.1. Design of the Coupled Inductor

To achieve ripple-free conditions, the converter should operate in CCM mode which means the current i_L must be continuous. Thus, combining the current waveform in Figure 4 and (13), the minimum value $I_{Lm,min}$ should be greater than zero. Equation (13) can also be written as follows:

$$I_{Lm,\min} = I_{Lm}(1+\frac{\lambda}{2}) - \frac{V_{C1}-V_{in}}{L_m}(1-D)T_S \tag{35}$$

where λ is the ripple rate of the current i_{Lm}.

Since the average current I_{Lk} is zero, the average current on the primary side of the coupled inductor is also zero. The average current I_{Lm} can be expressed by

$$I_{Lm} = I_{in} \tag{36}$$

Combining (4), (35), and (36), the minimum value of L_m can be obtained below:

$$L_{m,\min} = \frac{2V_{in}T_S D}{(2+\lambda)I_{in}} \tag{37}$$

Therefore, to ensure that the circuit operates under CCM mode, L_m should be selected with the following condition:

$$L_m > L_{m,\min} \tag{38}$$

When the value of L_m is determined, L_k can be determined by (11).

5.2. Design of Capacitors

In mode 1, the current flowing through C_0 is i_{Lk}. The currents flowing through C_3, C_4, and C_7 are i_{D3}, i_{D4}, and i_{D7}, respectively. Assuming that the capacitor voltage ripple rate is $x_c\%$, the minimum values of the capacitors C_3, C_4, and C_7 can be obtained from the capacitor's characteristic equation as follows:

$$C_{n\min} = \int_0^{DT_S} \frac{i_{Dn}}{x_c\% V_{Cn}} dt \tag{39}$$

and C_{0min} can be expressed by

$$C_{0\min} = \int_0^{DT_S} \frac{i_{Lk}}{x_c\% V_{C0}} dt \tag{40}$$

Similarly, in mode 2, the currents flowing through C_1, C_2, C_5, and C_6 are i_{D1}, i_{D2}, i_{D5}, and i_{D6}, respectively. Thus, the minimum values of the capacitors C_1, C_2, C_5, and C_6 can be obtained as follows:

$$C_{n\min} = \int_{DT_S}^{T_S} \frac{i_{Dn}}{x_c\% V_{Cn}} dt \tag{41}$$

5.3. Selection of Switch and Diodes

For switch S and diodes D_1-D_7, according to the voltage stress relationship obtained from (22) and considering an appropriate margin, the maximum withstand voltage value is given below:

$$V_{DS} = V_{D1} = V_{D2} = V_{D3} = V_{D4} = V_{D5} = V_{D6} = V_{D7} = \frac{k_V V_{in}}{1-D} \tag{42}$$

where k_V represents the voltage margin factor.

6. Experimental Results

To verify the validity and feasibility of the proposed topology, a 240 W laboratory prototype converter at 35 kHz switching frequency was designed. Detailed parameters and selected components are given in Table 2. Since the experimental leakage inductance of the coupled inductor was about 2 uH, an auxiliary inductor was connected in series with the secondary side of the coupled inductor to meet the requirements. The main voltage and current experimental waveforms of the converter are shown in Figure 11.

Table 2. Parameters of the converter.

Parameters	Value/Model
Input voltage V_{in}/V	40
Output voltage V_O/V	308
Switching frequency f_S/kHz	35
Magnetic inductor L_m/uH	250
Leakage inductance L_k/uH	62.5
Turn ratio n	1:2
Capacitor C_0/uF	330
Diodes D_1–D_7	MBR10200CT
Switch	IRFP260NPBF

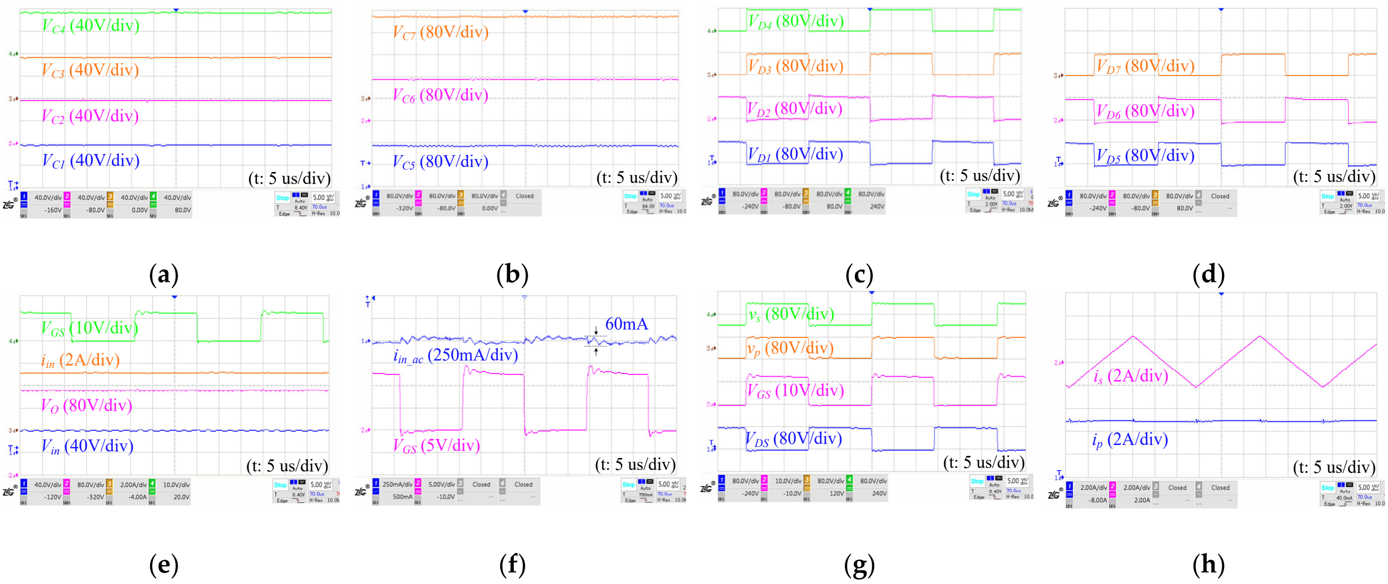

Figure 11. Experimental waveforms of the prototype: (**a**) V_{C1}, V_{C2}, V_{C3}, and V_{C4}; (**b**) V_{C5}, V_{C6}, and V_{C7}; (**c**) V_{D1}, V_{D2}, V_{D3}, and V_{D4}; (**d**) V_{D5}, V_{D6}, and V_{D7}; (**e**) V_{in}, V_O, i_{in}, and V_{GS}; (**f**) $i_{in\text{-}ac}$, and V_{GS}; (**g**) V_S, V_{GS}, v_p, and v_s; (**h**) i_p and i_s.

From Figure 11a, V_{C1}–V_{C4} reach nearly 80 V. Due to the R_{DSon} of the switch and the forward voltage drop of the diodes, V_{C1}–V_{C4} are slightly lower than the theoretical values. From Figure 11b, V_{C5} and V_{C6} reach nearly 160 V, and V_{C7} reaches nearly 320 V. Due to the loss of devices on different loops, V_{C5}–V_{C7} are also slightly lower than the theoretical values.

From Figure 11c,d, the voltage stresses on the diodes D_1–D_7 are about 80 V which is consistent with the theoretical analysis. Figure 11e shows that the output voltage reaches up to 308 V under 40 V input voltage. Hence, the experimental results verify that the proposed converter has the characteristic of high voltage gain. According to the theoretical calculation, the output voltage should have been 320 V under ideal conditions. The difference between experimental results and ideal conditions is caused by the non-idealities in the circuit. As can be seen from the waveform of i_{in} in Figure 11e, the input current i_{in} is constant. The ac component of i_{in} shown in Figure 11f is about 60 mA. The ripple rate of i_{in} is only 1.1%, thus the proposed converter provides a ripple-free input current through the aforementioned parameter design. From Figure 11g, the voltages at both ends of the primary and secondary sides of the coupled inductor change at the same time and have the same value. Figure 11h shows the currents of the coupled inductor, where i_p and i_s represent the current on the primary and secondary sides of the coupled inductor, respectively. Also, the voltage and current waveforms of the coupled inductor in Figure 11g,h are consistent with the theoretical waveforms in Figure 4.

In summary, the experimental results verify the validity and feasibility of the proposed converter. Some deviations from the theoretical analysis are inevitable. The proposed converter exhibits an efficiency of 93.7% at a 240 W load. Figure 12 shows the measured efficiency curve of the proposed converter under different loads and the maximum efficiency is 94.5%. Figure 13 shows the photograph of the experimental prototype.

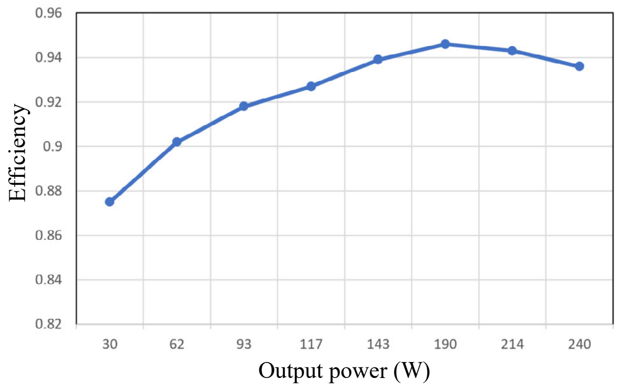

Figure 12. Measured efficiency of the proposed converter.

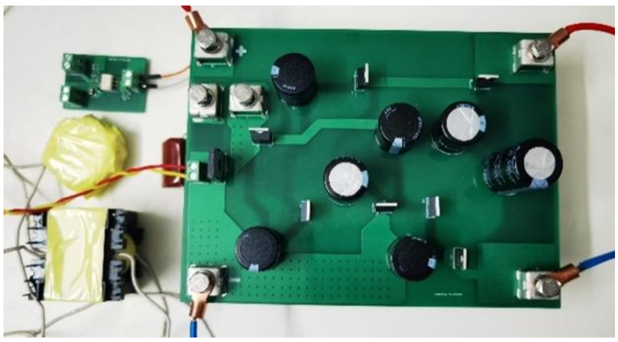

Figure 13. Photograph of the experimental prototype.

7. Conclusions

Aiming at the MVDC system in offshore wind farms, a novel single-switch high-gain dc/dc converter with a ripple-free input current is proposed in this paper. Since the converter uses only one switch, the control strategy is not complicated which is beneficial for the stability of offshore wind energy systems. The converter provides a high voltage gain through a switched-capacitor structure. Additionally, the converter provides a ripple-free input current by utilizing a coupled inductor which can avoid the use of a large electrolytic capacitor. Hence, the volume and weight of the converter are reduced. Moreover, the output capacitor is charged and discharged continuously by a 180° phase shift to eliminate output voltage ripple which can further improve the stability of the systems. The steady-state characteristic under CCM of the converter is analyzed. Comparisons of the proposed converter with its counterparts show various beneficial characteristics as follows: (1) high voltage gain; (2) ripple-free input current; (3) simple control strategy; (4) low voltage stress on devices; and (5) high efficiency. Finally, to verify the validity and feasibility of the proposed converter, a laboratory prototype has been built for a power of 240 W, input and output voltages of 40 and 308 V, respectively, and a switching frequency of 35 kHz. The input current ripple is only 1.1% and the maximum efficiency is measured to be 94.5%.

Experimental results confirm that the proposed converter is well suited for high-gain offshore wind energy applications.

Author Contributions: Conceptualization, R.T. and J.Y.; methodology, R.T. and Z.L.; software, Z.H.; validation, Z.L. and J.L.; formal analysis, Z.L.; investigation, R.A.; resources, R.A.; data curation, Z.H.; writing—original draft preparation, R.T. and Z.L.; writing—review and editing, J.L. and J.Y.; project administration, J.L. All authors have read and agreed to the published version of the manuscript.

Funding: This research was supported by the Open Fund of Guangdong Key Laboratory of New Technology for Smart Grid under GDDKY2021KF02.

Institutional Review Board Statement: Not applicable.

Informed Consent Statement: Not applicable.

Data Availability Statement: Not applicable.

Conflicts of Interest: The authors declare no conflict of interest.

References

1. Fjellstedt, C.; Ullah, M.I.; Forslund, J.; Jonasson, E.; Temiz, I.; Thomas, K. A Review of AC and DC Collection Grids for Offshore Renewable Energy with a Qualitative Evaluation for Marine Energy Resources. *Energies* **2022**, *15*, 5816. [CrossRef]
2. Lam, J.; Jain, P.K. A High Efficient Medium Voltage Step-up DC/DC Converter with Zero Voltage Switching (ZVS) and Low Voltage Stress for Offshore Wind Energy Systems. In Proceedings of the 2014 16th European Conference on Power Electronics and Applications, Lappeenranta, Finland, 26–28 August 2014; IEEE: Piscataway, NJ, USA, 2014; pp. 1–10.
3. Lee, Y.; Vakil, G.; Feldman, R.; Watson, A.J.; Wheeler, P.W. A High-Power DC-DC Converter Based Dual Active Bridge for MVDC Grids on Offshore Wind Farms. In Proceedings of the 2016 18th European Conference on Power Electronics and Applications (EPE'16 ECCE Europe), Karlsruhe, Germany, 5–9 September 2016; IEEE: Piscataway, NJ, USA, 2016; pp. 1–10.
4. Abeynayake, G.; Van Acker, T.; Hertem, D.V.; Liang, J. Analytical Model for Availability Assessment of Large-Scale Offshore Wind Farms Including Their Collector System. *IEEE Trans. Sustain. Energy* **2021**, *12*, 1974–1983. [CrossRef]
5. Basbas, H.; Liu, Y.-C.; Laghrouche, S.; Hilairet, M.; Plestan, F. Review on Floating Offshore Wind Turbine Models for Nonlinear Control Design. *Energies* **2022**, *15*, 5477. [CrossRef]
6. Wang, B.; Tian, M.; Lin, T.; Hu, Y. Distributed Complementary Control Research of Wind Turbines in Two Offshore Wind Farms. *Sustainability* **2018**, *10*, 553. [CrossRef]
7. Vagiona, D.; Kamilakis, M. Sustainable Site Selection for Offshore Wind Farms in the South Aegean—Greece. *Sustainability* **2018**, *10*, 749. [CrossRef]
8. Torres, J.P.N.; De Jesus, A.S.; Marques Lameirinhas, R.A. How to Improve an Offshore Wind Station. *Energies* **2022**, *15*, 4873. [CrossRef]
9. Bernal-Camacho, D.F.; Fontes, J.V.H.; Mendoza, E. A Technical Assessment of Offshore Wind Energy in Mexico: A Case Study in Tehuantepec Gulf. *Energies* **2022**, *15*, 4367. [CrossRef]
10. Rong, F.; Wu, G.; Li, X.; Huang, S.; Zhou, B. ALL-DC Offshore Wind Farm With Series-Connected Wind Turbines to Overcome Unequal Wind Speeds. *IEEE Trans. Power Electron.* **2019**, *34*, 1370–1381. [CrossRef]
11. Bahmani, M.A.; Thiringer, T.; Rabiei, A.; Abdulahovic, T. Comparative Study of a Multi-MW High-Power Density DC Transformer with an Optimized High-Frequency Magnetics in All-DC Offshore Wind Farm. *IEEE Trans. Power Delivery* **2016**, *31*, 857–866. [CrossRef]
12. Hu, P.; Yin, R.; Wei, B.; Luo, Y.; Blaabjerg, F. Modular Isolated LLC DC/DC Conversion System for Offshore Wind Farm Collection and Integration. *IEEE J. Emerg. Sel. Top. Power Electron.* **2021**, *9*, 6713–6725. [CrossRef]
13. Herrera, D.; Tricarico, T.; Oliveira, D.; Aredes, M.; Galván-Díez, E.; Carrasco, J.M. Advanced Local Grid Control System for Offshore Wind Turbines with the Diode-Based Rectifier HVDC Link Implemented in a True Scalable Test Bench. *Energies* **2022**, *15*, 5826. [CrossRef]
14. Xie, L.; Cheng, F.; Wu, J. Control Strategy for Offshore Wind Farms with DC Collection System Based on Series-Connected Diode Rectifier. *Sustainability* **2022**, *14*, 7860. [CrossRef]
15. Liu, H.; Dahidah, M.; Naayagi, R.T.; Armstrong, M.; Yu, J. Unidirectional DC/DC Modular Multilevel Converter for Offshore Windfarm with the Control Strategy Based on Stationary Frame. *J. Eng.* **2019**, *2019*, 4309–4314. [CrossRef]
16. Liu, J.; Li, B.; Li, L.; Liu, X.; Wu, J.; Xu, D.; Wei, T.; Li, W. A High Step-up Ratio DC-DC Converter with Fault Blocking Capability for Offshore Wind Farms. In Proceedings of the 2021 IEEE 12th Energy Conversion Congress & Exposition-Asia (ECCE-Asia), Singapore, 24 May 2021; IEEE: Singapore, 2021; pp. 702–707.
17. Dincan, C.; Kjaer, P.; Chen, Y.; Munk-Nielsen, S.; Bak, C.L. Analysis of a High-Power, Resonant DC–DC Converter for DC Wind Turbines. *IEEE Trans. Power Electron.* **2018**, *33*, 7438–7454. [CrossRef]
18. Zhao, X.; Li, B.; Zhang, B.; Xu, D. A High-Power Step-Up DC/DC Converter Dedicated to DC Offshore Wind Farms. *IEEE Trans. Power Electron.* **2022**, *37*, 65–69. [CrossRef]

19. Deng, F.; Chen, Z. Control of Improved Full-Bridge Three-Level DC/DC Converter for Wind Turbines in a DC Grid. *IEEE Trans. Power Electron.* **2013**, *28*, 314–324. [CrossRef]
20. Chen, W.; Huang, A.; Lukic, S.; Svensson, J.; Li, J.; Wang, Z. A Comparison of Medium Voltage High Power DC/DC Converters with High Step-up Conversion Ratio for Offshore Wind Energy Systems. In Proceedings of the 2011 IEEE Energy Conversion Congress and Exposition, Phoenix, AZ, USA, 17–22 September 2011; IEEE: Piscataway, NJ, USA, 2011; pp. 584–589.
21. Liu, H.; Dahidah, M.S.A.; Yu, J.; Naayagi, R.T.; Armstrong, M. Design and Control of Unidirectional DC–DC Modular Multilevel Converter for Offshore DC Collection Point: Theoretical Analysis and Experimental Validation. *IEEE Trans. Power Electron.* **2019**, *34*, 5191–5208. [CrossRef]
22. Denniston, N.; Massoud, A.M.; Ahmed, S.; Enjeti, P.N. Multiple-Module High-Gain High-Voltage DC–DC Transformers for Offshore Wind Energy Systems. *IEEE Trans. Ind. Electron.* **2011**, *58*, 1877–1886. [CrossRef]
23. Parastar, A.; Seok, J.-K. High-Gain Resonant Switched-Capacitor Cell-Based DC/DC Converter for Offshore Wind Energy Systems. *IEEE Trans. Power Electron.* **2015**, *30*, 644–656. [CrossRef]
24. Banaei, M.R.; Sani, S.G. Analysis and Implementation of a New SEPIC-Based Single-Switch Buck–Boost DC–DC Converter With Continuous Input Current. *IEEE Trans. Power Electron.* **2018**, *33*, 10317–10325. [CrossRef]
25. Saravanan, S.; Babu, N.R. Design and Development of Single Switch High Step-Up DC–DC Converter. *IEEE J. Emerg. Sel. Topics Power Electron.* **2018**, *6*, 855–863. [CrossRef]
26. Gandomkar, A.; Parastar, A.; Seok, J.-K. High-Power Multilevel Step-Up DC/DC Converter for Offshore Wind Energy Systems. *IEEE Trans. Ind. Electron.* **2016**, *63*, 7574–7585. [CrossRef]
27. Hu, Y.; Zeng, R.; Cao, W.; Zhang, J.; Finney, S.J. Design of a Modular, High Step-Up Ratio DC–DC Converter for HVDC Applications Integrating Offshore Wind Power. *IEEE Trans. Ind. Electron.* **2016**, *63*, 2190–2202. [CrossRef]
28. Abbasi, M.; Lam, J. A Step-Up Transformerless, ZV–ZCS High-Gain DC/DC Converter With Output Voltage Regulation Using Modular Step-Up Resonant Cells for DC Grid in Wind Systems. *IEEE J. Emerg. Sel. Topics Power Electron.* **2017**, *5*, 1102–1121. [CrossRef]
29. Parastar, A.; Kang, Y.C.; Seok, J.-K. Multilevel Modular DC/DC Power Converter for High-Voltage DC-Connected Offshore Wind Energy Applications. *IEEE Trans. Ind. Electron.* **2015**, *62*, 2879–2890. [CrossRef]
30. Yin, R.; Shi, M.; Hu, W.; Guo, J.; Hu, P.; Wang, Y. An Accelerated Model of Modular Isolated DC/DC Converter Used in Offshore DC Wind Farm. *IEEE Trans. Power Electron.* **2019**, *34*, 3150–3163. [CrossRef]
31. Zhang, J.; Sha, D.; Ma, P. A Dual Active Bridge DC–DC-Based Single Stage AC–DC Converter With Seamless Mode Transition and High Power Factor. *IEEE Trans. Ind. Electron.* **2022**, *69*, 1411–1421. [CrossRef]
32. García-Vite, P.M.; Rosas-Caro, J.C.; Martínez-Salazar, A.L.; Chavez, J.d.J.; Valderrábano-González, A.; Sánchez-Huerta, V.M. Quadratic Buck–Boost Converter with Reduced Input Current Ripple and Wide Conversion Range. *IET Power Electron.* **2019**, *12*, 3977–3986. [CrossRef]
33. Do, H.-L. Improved ZVS DC-DC Converter With a High Voltage Gain and a Ripple-Free Input Current. *IEEE Trans. Circuits Syst. I* **2012**, *59*, 846–853. [CrossRef]
34. Yang, N.; Zeng, J.; Hu, R.; Liu, J. Analysis and Design of an Isolated High Step-Up Converter Without Voltage-Drop. *IEEE Trans. Power Electron.* **2022**, *37*, 6939–6950. [CrossRef]
35. Liu, J.; Lin, W.; Wu, J.; Zeng, J. A Novel Nine-Level Quadruple Boost Inverter With Inductive-Load Ability. *IEEE Trans. Power Electron.* **2019**, *34*, 4014–4018. [CrossRef]